Redox-network reconfiguration inferred from the $\ln[O_2]$–E_h relationship under mixed-potential conditions in a shallow pond time series

Kyoko Morimoto[1], Mana Ito[2], Katsutoshi Ito[2], and Mayumi Seto[3]

[1]Department of Chemistry, Biology, and Environmental Sciences, Nara Womens University, Kita-Uoya Nishimachi, Nara 630-8506, Japan
[2]Environmental Conservation Division, Environment and Fisheries Applied Research Department, Fisheries Technology Institute, Japan Fisheries Research and Education Agency, 2-17-5 Maruishi, Hatsukaichi, Hiroshima 739-0452, Japan
[3]Department of Environmental and Natural Resource Sciences, Faculty of Agriculture, Tokyo University of Agriculture and Technology, 3-5-8 Saiwaicho, Fuchu-shi, Tokyo 183-8509, Japan

Correspondence: Mayumi Seto (seto@go.tuat.ac.jp)

Abstract. Oxidation–reduction potential (E_h) is widely used as an in situ indicator of redox conditions in aquatic environments, and field electrodes typically record a mixed potential generated by multiple concurrent interfacial redox reactions. Beyond a simple Nernstian interpretation based on a single redox couple, here we ask what mechanistic information can be extracted from an observed relationship between E_h and a single chemical species under mixed-potential conditions, focusing on dissolved oxygen. Using a linearized mixed-potential formulation, we show that the sensitivity $\partial E_h / \partial \ln a_x$ can be decomposed into (i) Nernstian contributions and (ii) kinetic contributions from multiple reactions. Consequently, an approximately constant log-linear $\ln[O_2]$–E_h sensitivity does not require dominance by a single couple (e.g., O_2/H_2O); it can also arise when the effective reaction set contributing to the mixed potential and their relative weights remain approximately invariant, suggesting that this relationship can serve as a compact indicator of redox-network stability.

To examine whether such slope stability and breakdown are observable in the field, we apply this interpretation to a 21-month, multi-site time series from a constructed shallow pond in Japan, where dissolved oxygen and electrode redox potential were co-measured at weekly fixed depths and along biweekly vertical profiles. Channel excavation produced a pond-wide electrical conductivity anomaly, and change-point detection was used to define pre- and post-disturbance regimes. During the pre-disturbance regime, the $\ln[O_2]$–E_h slope was relatively stable across sites. After disturbance, the inflow-proximal site exhibited a weakened slope and systematically elevated E_h relative to the pre-disturbance baseline; notably, baseline-referenced E_h deviations peaked after the EC anomaly had largely relaxed, and a follow-up survey in February 2025 indicated partial recovery. Co-located E_h and oxygen measurements can thus provide a simple, system-level indicator of disturbance-driven redox-network reconfiguration and recovery, while recognizing that comprehensive speciation remains necessary to identify the dominant redox couples.

1 Introduction

Redox processes regulate the transformations of carbon, nitrogen, sulfur, iron, and other redox-sensitive elements, thereby shaping nutrient cycling, organic-matter degradation, and the mobility and reactivity of heavy metals in aquatic environments (Borch et al., 2010; Violante et al., 2010; Schlesinger and Bernhardt, 2013; Tandon and Singh, 2016; Lau et al., 2018; Linnik et al., 2023). Oxidation–reduction potential (E_{h}) is therefore widely used as a convenient in situ indicator of oxidizing or reducing conditions in natural waters (Whitfield, 1969; Stumm and Morgan, 1996; Luther, 2016).

In natural waters, multiple redox couples coexist and exchange electrons at different rates under the combined influence of transport, chemical reactions, and microbial metabolism (Stefánsson et al., 2005; Grundl, 1994; Grenthe et al., 1992). These coupled processes constitute a redox reaction network that establishes concentration gradients of oxidants and reductants in the bulk solution and determines their local activities at the electrode surface (Fig. 1). As a result, field E_{h} measurements generally reflect a mixed potential, E_{mix}, at which the net interfacial current vanishes,

$$\sum_k i_k(E_{\mathrm{mix}}) = 0. \tag{1}$$

Here $i_k(E)$ denotes the partial current associated with reaction k at electrode potential E. Consequently, E_{h} cannot, in general, be interpreted as a quantitative proxy for any specific redox couple (e.g., Fe(III)/Fe(II), Mn(IV)/Mn(II), NO_3^-/NO_2^-, SO_4^{2-}/HS^-), nor for individual reaction fluxes. Consistent with this mixed-potential view, prior studies have shown that measured E_{h} does not necessarily track the Nernst (equilibrium) potentials of selected redox couples in natural waters (Whitfield, 1974; Lindberg and Runnells, 1984; Teasdale et al., 1998; Ramesh Kumar and Riyazuddin, 2012; Bowman et al., 2025).

Although mixed-potential theory does not, in general, ensure a one-to-one mapping between E_{h} and any single chemical species, in practice E_{h} often covaries with the activity of particular oxidants, reductants, or redox couples, and empirical relationships have been reported across diverse field settings (e.g., Seto and Akagi, 2005; Włodarczyk et al., 2007; Auqué et al., 2008; Winkel et al., 2008; Ioka et al., 2011; Jahangir et al., 2012; Zhai et al., 2012; McAleer et al., 2017; Silva et al., 2017; Aladejana et al., 2020; Cuoco et al., 2022). This raises a key question: under what mechanistic constraints can a seemingly simple E_{h}–species relationship arise from mixed-potential dynamics?

Here we revisit E_{h} explicitly as a mixed potential and ask what information can, and cannot, be extracted from its relationship with the activity of a single species. Rather than treating E_{h} as a proxy for a specific redox couple, we interpret it as a reduced-order observable emerging from a high-dimensional reaction network. Within this framework, we show that the sensitivity of E_{h} to $\ln[O_2]$ provides a compact indicator of the effective stability of the reaction set contributing to the mixed potential. Applying this approach to a 21-month time series from a constructed pond, we quantify site-dependent differences in redox-network stability and identify a disturbance-induced shift in $\ln[O_2]$–E_{h} sensitivity followed by gradual recovery.

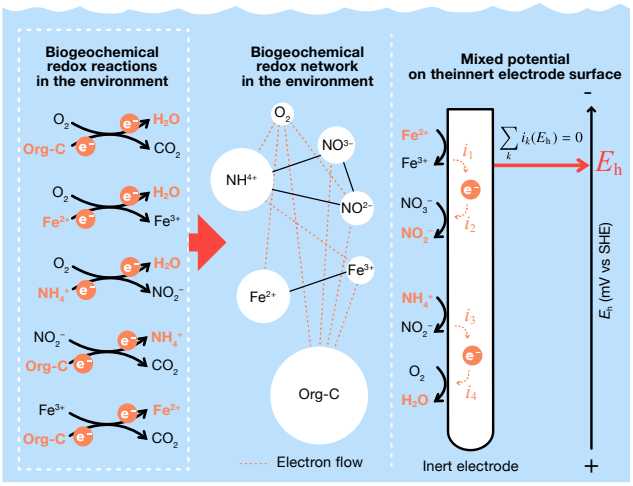

Figure 1. Conceptual schematic illustrating how E_{h} measured by an inert electrode emerges as a mixed potential from a biogeochemical redox reaction network. Left: Representative biogeochemical redox reactions in natural environments, in which multiple oxidants and reductants exchange electrons through microbial metabolism, chemical reactions, and transport processes. Middle: These reactions collectively form a redox reaction network that establishes electron flows and concentration gradients of redox-active species (e.g., O_2, NO_3^-, NO_2^-, Fe^{2+}/Fe^{3+}, NH_4^+, and organic carbon) in the bulk environment. Right: At the inert electrode surface, each redox couple contributes a partial current $i_k(E)$, and the measured potential E_{h} adjusts to a value at which the net interfacial current vanishes, $\sum_k i_k(E_{\mathrm{h}}) = 0$.

2 Materials and Methods

2.1 Monitoring site

A small artificial pond ($\approx 10\ \mathrm{m}^3$; 34°41′14.5″N, 135°49′45.9″E) in Nara Prefecture, Japan, served as the study site (Fig. 2). The pond is surrounded by trees and receives substantial inputs of leaf litter in autumn. The bottom substrate consists primarily of gravel mixed with decomposed leaves, and no aquatic macrophytes are present. Water depth varies spatially, exceeding 40 cm at Site A1 and A0, ranging from 20 to 40 cm at Site B, and remaining below 20 cm at Site C.

The pond is enclosed on three sides by a waterproof mortar structure that prevents lateral inflow or outflow. To promote water circulation, channel-construction works were conducted twice: an initial manual excavation in August 2022, followed by a larger-scale mechanical excavation in May–June 2023. After channel construction, water was pumped intermittently (daytime only) using a solar-powered system. Pumping volumes measured during 26 August–14 September 2022 averaged 499 L day^{-1} (range: 124–1300 L day^{-1}). Following the June 2023 excavation, sediment-laden inflow from freshly disturbed soils was observed to enter the pond (Fig. 2c).

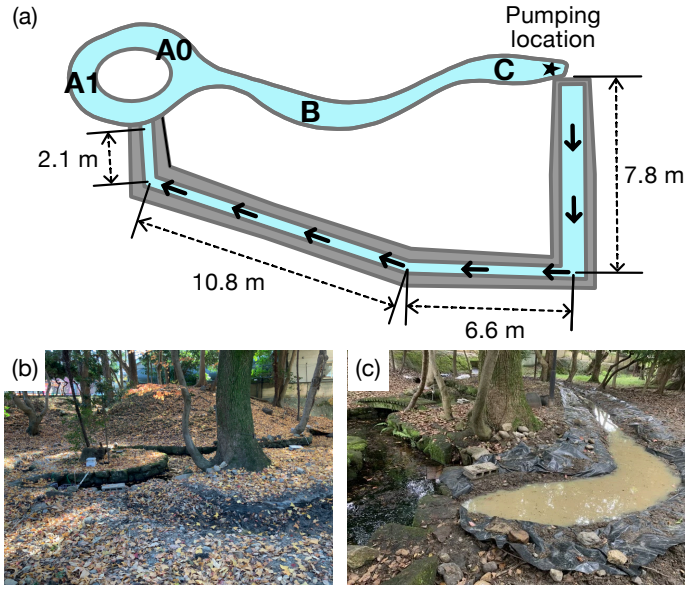

Figure 2. Overview of the constructed pond and sampling locations. (a) Schematic plan view showing the positions of monitoring sites A1, A0, B, and C, together with the artificial channel and pumping location. Arrows indicate the direction of water flow driven by intermittent pumping, and distances between segments are provided for scale. (b) Photograph of the pond environment illustrating the forested setting and substantial leaf-litter accumulation around the pond. (c) Photograph taken on 15 June 2023 after construction of the peripheral channel, showing sediment-laden inflow that represents the major physical disturbance analyzed in this study.

2.2 Weekly stationary and biweekly vertical profile monitoring

From July 2022 to March 2024, water-quality monitoring was conducted weekly at four sites (A0, A1, B, and C) using portable instruments. Site A1 was monitored throughout the study period (7 July 2022 to 30 March 2024) as the primary reference site, whereas Sites A0, B, and C were monitored during partially overlapping intervals due to logistical constraints. A follow-up vertical-profile survey was additionally conducted in February 2025 using the same instrument and protocols.

At each site, measurements were taken at two depths (5 cm below the water surface and near the bottom) on a weekly basis. In addition, vertical profiles were obtained at 5 cm intervals from the water surface downward every two weeks. All measurements were performed between 10:00 and 15:00 (local time).

Measured parameters were pH, dissolved oxygen (DO), oxidation–reduction potential (ORP, reported as E_h), electrical conductivity (EC), water temperature, and water depth. pH was measured using a PRN-41 (Fujiwara Scientific Co., Ltd., Japan), and water depth was measured using a measuring stick. DO, ORP, EC, and water temperature were measured using a LAQUA-WQ310 (Horiba Scientific, Japan). The DO optode was model 300-D-2, the ORP electrode was model 9300-10D (reference electrode: 3.33 mol L^{-1} KCl Ag/AgCl; indicator electrode: Pt), and the EC electrode was model 300-C-2 (sensor head) equipped with a 300-4C-C cartridge. Manufacturer specifications (measurement range, resolution, and stated accura-

cy/repeatability) for all sensors are summarized in Supplementary Table A1. The pH and DO sensors were calibrated before each field survey following the manufacturers protocols. The ORP and EC sensors were checked against standard solutions prior to the start of the monitoring period, but were not routinely recalibrated thereafter. Before each survey, electrodes were rinsed with distilled water, gently agitated, and visually inspected for deposits. The same instrument and electrodes were used throughout the monitoring period. All measurements were performed in situ without sample collection to minimize redox alteration during handling. Readings were recorded only after the instrument indicated stabilization, which typically required several minutes and occasionally up to ∼20 min.

ORP values were converted to standard hydrogen electrode-based values (mV vs. SHE) using the manufacturer-recommended conversion for a 3.33 mol L^{-1} KCl Ag/AgCl reference electrode and corrected for temperature:

$$E_{\mathrm{h}}\ (\mathrm{mV}) = E_{\mathrm{Ag/AgCl}}\ (\mathrm{mV}) + 206 - 0.7\,(T - 25), \tag{2}$$

assuming a temperature coefficient of -0.7 mV $^{\circ}C^{-1}$ for the Ag/AgCl reference electrode. $E_{\mathrm{Ag/AgCl}}$ is the measured potential (mV) relative to the Ag/AgCl reference electrode and T is temperature ($^{\circ}$C).

DO (mg L^{-1}) was converted to molar concentration using the molar mass of O_2 (31.998 g mol^{-1}), and the resulting concentration was used as a proxy for O_2 activity. The activity of O_2 was approximated by its molar concentration for all analyses, and $\ln[O_2]$ denotes the natural logarithm (base e). Because $\ln[O_2]$ requires strictly positive values, DO readings reported as 0.00 mg L^{-1} were excluded from log-transformed analyses; all values $>$0.00 mg L^{-1} were retained.

3 Results

3.1 Implications of a constant E_{h} sensitivity under mixed-potential control

To interpret the mechanistic meaning of an observed E_{h}–species relationship under mixed-potential conditions, we derive when an approximately constant sensitivity of E_{h} to the logarithm of a species activity can arise.

E_{h} represents a mixed potential arising from multiple interfacial electrochemical reactions. Under open-circuit conditions, the electrode potential adjusts so that the net interfacial current vanishes due to the balance of partial currents (Eq. (1)). For each reaction k, the (Nernst) equilibrium potential E_k is defined by $i_k(E_k) = 0$ under electrochemical equilibrium and follows the Nernst equation. Assuming that E_{mix} lies sufficiently close to E_k for the reactions that contribute appreciably to the zero-current balance, we linearize the partial current about E_k (Appendix A) to obtain

$$i_k(E) \simeq G_k(E - E_k), \tag{3}$$

where G_k is the partial polarization conductance. This assumption is self-consistent because any reaction with appreciable G_k cannot sustain a large overpotential at open circuit without generating a large partial current that would violate the zero-current balance. Substituting this into the zero-current condition yields

$$E_{\mathrm{mix}} = \frac{\sum_k G_k E_k}{\sum_k G_k}. \tag{4}$$

Thus, within the linear polarization regime, the mixed potential is a conductance-weighted average of the equilibrium potentials of the contributing reactions.

We next differentiate Eq. (4) with respect to $x = \ln a_x$. Defining normalized conductance weights as $w_k = G_k / \sum_j G_j$ (so that $\sum_k w_k = 1$), we obtain

$$\frac{\partial E_{\mathrm{mix}}}{\partial x} = \sum_k w_k \frac{\partial E_k}{\partial x} + \sum_k w_k (E_k - E_{\mathrm{mix}}) \frac{\partial \ln G_k}{\partial x}. \tag{5}$$

Equation (5) decomposes the sensitivity into (i) a weighted sum of Nernst contributions, through $\partial E_k / \partial x$, and (ii) a kinetic reweighting contribution that arises when the relative polarization conductances change with x. The second (reweighting) term is suppressed when the relative conductance weights are nearly invariant with x over the range of interest, i.e., when $\partial \ln G_k / \partial x$ is approximately common across the contributing reactions (equivalently, w_k varies weakly with x). In that case, Eq. (5) reduces to

$$\frac{\partial E_{\mathrm{mix}}}{\partial x} \approx \sum_k w_k \frac{\partial E_k}{\partial x}. \tag{6}$$

In the limiting case where a single reaction dominates the polarization conductance ($w_d \simeq 1$), the mixed potential approaches its equilibrium potential ($E_{\mathrm{mix}} \simeq E_d$) and $\partial E_{\mathrm{mix}} / \partial x \simeq \partial E_d / \partial x$. From the Nernst equation, $\partial E_d / \partial \ln a_x$ is set by $(RT/n_d F)$ multiplied by the stoichiometric coefficient of x in the reaction quotient (with the sign determined by whether x appears as an oxidant or reductant), yielding an approximately constant log-linear sensitivity. Importantly, Eq. (5) also shows that an approximately constant E_{h} sensitivity to $\ln a_x$ does not require single-couple dominance. It can equally reflect a multi-reaction mixed potential whose effective reaction set and relative weights remain approximately stable. Accordingly, an approximately consistent species–E_{h} slope can be interpreted as evidence that the effective redox-reaction set contributing to the mixed potential, and its relative weighting, remained broadly stable over the range of interest. Conversely, a systematic deviation from this slope points to disturbance-driven reorganization of the interfacial redox contributions sensed by the electrode, rather than a direct signature of the Nernst potential of a single redox couple.

3.2 Disturbance-driven EC anomaly and change-point detection

We tested this interpretation using a shallow pond time series that experienced a clearly documented disturbance associated with channel excavation. Such a disturbance can affect not only oxygen availability and measured E_{h} , but also the effective redox-reaction network near the electrode and thereby disrupt the $\ln[\mathrm{O_2}]$–E_{h} relationship. We used electrical conductivity (EC) as a proxy for disturbance because sediment mobilization and the exposure of fresh mineral surfaces can enhance ion release via accelerated weathering, producing detectable EC anomalies (Hayashi, 2004; Shrestha and Lal, 2011; Yu et al., 2012).

Following the mechanical excavation of the circulation channel in May–June 2023, EC exhibited a synchronous and pronounced increase across all monitoring sites (A1, A0, B, and C; Fig. 3a). Because monitoring began in July 2022, we cannot fully assess whether EC showed a recurring early-summer increase in the previous year (e.g., due to evapoconcentration during warm and dry periods). Nevertheless, EC during June–August 2023 clearly exceeded the baseline level: values were above the

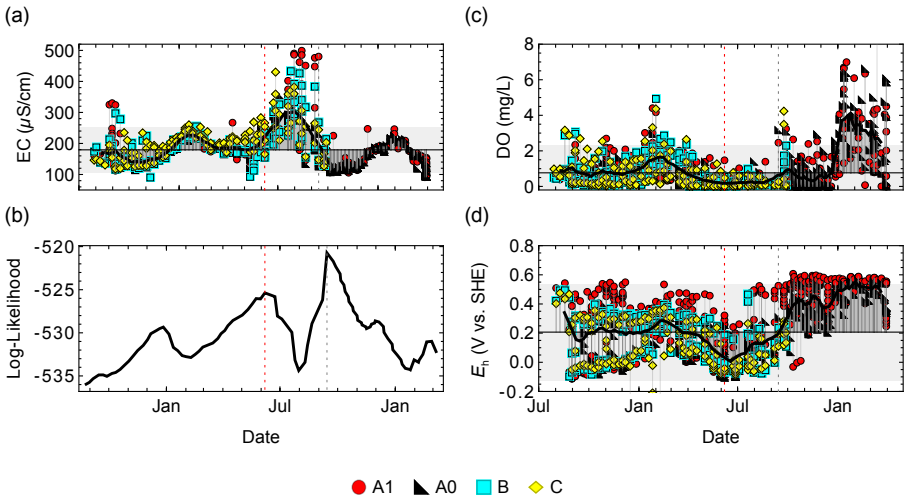

Figure 3. Disturbance-driven EC anomaly and likelihood-based change-point detection. (a) Weekly electrical conductivity (EC) at four monitoring sites (A1, A0, B, and C). (b) Log-likelihood profile of the two-segment Gaussian model applied to the EC time series at Site A1. (c) Dissolved oxygen (DO) time series. (d) Redox potential (E_h , vs. SHE) time series. Vertical dashed lines mark the operational change points adopted in the main text (red: disturbance onset associated with channel excavation; gray: transition from the EC amplification phase to the relaxation phase). Solid lines and shaded bands indicate the mean and mean ± 1.96 SD range during pre-disturbance regime calculated from all sites.

baseline mean and outside the 95% range estimated as ± 1.96 SD from observations collected prior to the completion of the excavation works (all sites pooled; 7 July 2022–7 June 2023). The largest increase was observed at Site A1, located closest to the inflow pathway, whereas the response at Site A0 was less pronounced, consistent with partial hydrodynamic shielding by the pond geometry (Fig. 2a). Thereafter, EC declined and returned to the baseline range within approximately three months. Overall, the EC record suggests a three-phase trajectory consisting of disturbance onset, transient amplification, and subsequent relaxation.

To objectively identify the timing of disturbance onset, we applied change-point detection to the weekly EC time series using a two-segment Gaussian likelihood model, where each segment has its own mean and variance. For each candidate change point t_{change}, we computed the joint log-likelihood of the EC observations by fitting the model separately to the pre- and post-change segments. Because Sites B and C include substantial data gaps after the disturbance period, which can introduce spurious likelihood maxima, the change-point analysis was performed for Site A1 only (the primary reference site) and for the mean EC series across Sites A1 and A0, yielding consistent likelihood profiles (Fig. 3b). Local maxima in the likelihood profile were identified using the FindPeaks function in Wolfram Language.

The global maximum of the likelihood corresponded to a change point separating the amplification phase from the subsequent relaxation phase (Fig. 3b). A second prominent peak coincided with the completion date of the channel excavation works (7 June 2023), indicating the transition from baseline conditions to the disturbance-driven EC increase. Because our primary

objective is to define the onset of disturbance, we adopt this second peak as the operational change point and refer to the period prior to this date as the pre-disturbance regime and the subsequent period as the post-disturbance regime.

Dissolved oxygen (DO) tended to increase during the latter part of the post-disturbance regime relative to the same season in the previous year (Fig. 3c), likely reflecting enhanced air–water mixing associated with inflow events. Consistent with this trend, E_{h} exhibited an overall upward shift following the disturbance (Fig. 3d). Notably, during the pre-disturbance period E_{h} often showed vertical separation between surface and bottom waters, whereas this vertical divergence became less pronounced after the disturbance, consistent with enhanced vertical mixing.

Temperature showed typical seasonal cycles and vertical structure over the observation period, and pH ranged from 5.79 to 7.35 (mean 6.60) (Supplementary Fig. A1).

3.3 Stability and breakdown of the ln[O_2]–E_{h} relationship

For the analyses below, DO was converted to molar concentration and used as a proxy for O_2 activity; $\ln[\mathrm{O_2}]$ denotes the natural logarithm (base e). Because $\ln[\mathrm{O_2}]$ is defined only for strictly positive values, DO records reported as 0.00 mg L^{-1} were excluded from log-transformed analyses (see Methods for details).

During the pre-disturbance regime, a moderate positive relationship between $\ln[\mathrm{O_2}]$ and E_{h} was consistently observed across sites (pooled regression: E_{h} = 0.086 $\ln[\mathrm{O_2}]$ + 1.18; adjusted R^2 = 0.45; Fig. 4a). Site-specific slopes varied within a narrow range (0.072–0.105), and adjusted R^2 values were 0.47–0.52, with the highest value at Site A1 (Supplementary Table A2). Despite strong seasonal variability in temperature and oxygen availability, the pre-disturbance data therefore exhibit a broadly consistent $\partial E_h/\partial \ln[\mathrm{O_2}]$ across sites, consistent with a relatively stable effective redox-reaction structure over this period.

When the full observation period was considered, the $\ln[\mathrm{O_2}]$–E_{h} relationship at Site A1 weakened. The adjusted R^2 decreased by 0.124 relative to the pre-disturbance regression, indicating a loss of explanatory power. Site A1 is located closest to the inflow pathway and was most strongly affected by the sediment-mobilizing disturbance, suggesting a disturbance-driven modification of local redox conditions. Consistently, the slope at Site A1 decreased from 0.105 (pre-disturbance) to 0.083 (post-disturbance). Moreover, many post-disturbance observations at Site A1 lay above the 95% prediction interval of the pre-disturbance regression, indicating a systematic elevation of E_{h} relative to the expected $\ln[\mathrm{O_2}]$–E_{h} relationship.

Enhanced vertical mixing after disturbance could reduce surface–bottom E_{h} separation and thereby shift the observed relationship. However, the persistence of elevated E_{h} even under low O_2 conditions suggests that the change is unlikely to be explained solely by physical mixing, indicating an altered sensitivity of E_{h} to oxygen availability following redox-network reconfiguration. Importantly, a follow-up vertical-profile survey in February 2025 showed that the pre-disturbance $\ln[\mathrm{O_2}]$–E_{h} relationship at Site A1 partially re-emerged (orange points in Fig. 4a), suggesting gradual recovery of the pre-disturbance redox structure.

To quantify deviations from the pre-disturbance system-level relationship, we computed residuals $\Delta E_h = E_h^{\mathrm{obs}} - E_h^{\mathrm{pred,pooled}}$, where $E_h^{\mathrm{pred,pooled}}$ is the value predicted from the pooled pre-disturbance regression (Fig. 4b). Site A1 showed a pronounced positive shift in ΔE_h after disturbance, with the largest deviation occurring approximately three months after the EC peak. To compare pre- and post-disturbance residuals, we used a two-sample Students t-test when residuals were approximately

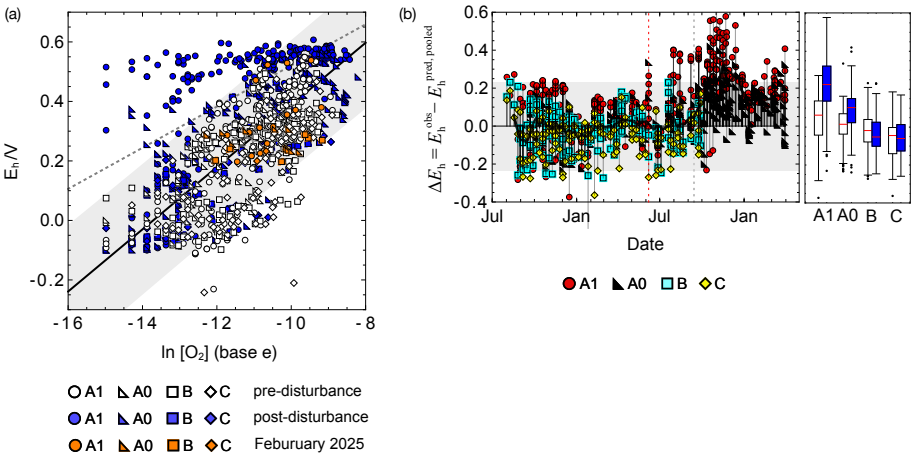

Figure 4. Disturbance-induced breakdown and recovery of the $\ln[O_2]$–E_h relationship. (a) Relationship between E_h (V vs. SHE) and $\ln[O_2]$ (natural logarithm; base e) across Sites A1, A0, B, and C. Open symbols indicate the pre-disturbance regime and filled symbols indicate the post-disturbance regime; orange symbols denote the February 2025 follow-up vertical-profile survey. The solid and dashed lines show the pre- and post-disturbance regressions at Site A1, respectively. The shaded band represents the 95% prediction interval of the pre-disturbance A1 regression. (b) Time series of residuals, $\Delta E_h = E_h^{obs} - E_h^{pred,pooled}$, where $E_h^{pred,pooled}$ was calculated from the pooled pre-disturbance regression. Vertical dashed lines mark the operational change points adopted in the main text (red: disturbance onset associated with channel excavation; gray: transition from the EC amplification phase to the relaxation phase). Boxplots summarize residual distributions for each site in the pre- (white) and post-disturbance (blue) regimes.

normally distributed with no strong evidence of unequal variances (Sites A0 and C); otherwise we used the nonparametric MannWhitney U test (Sites A1 and B). Significant differences were detected at Sites A1 and A0 ($p < 0.05$), whereas Sites B and C showed no significant difference, partly reflecting reduced sampling frequency after October due to logistical constraints.

4 Discussion

4.1 Mixed-potential interpretation of the observed slope breakdown

Field observations showed a relatively stable $\ln[O_2]$–E_h relationship during the pre-disturbance regime across sites, followed by a disturbance-associated weakening and reorganization of the relationship, most clearly at Site A1 where sediment-laden inflow was strongest (Fig. 4a). Here we interpret these patterns in terms of mixed-potential control and clarify what is inferred from an observed $\ln[O_2]$–E_h slope.

In the linearized mixed-potential framework (Eq. (5) with $x = \ln a_{O_2}$), the sensitivity $\partial E_h / \partial \ln a_{O_2}$ reflects two components: a multi-reaction Nernst contribution through $\partial E_k / \partial \ln a_{O_2}$ and a contribution from changes in the relative conductance weights of the reactions that collectively form the mixed potential. Importantly, an approximately constant $\ln[O_2]$–E_h slope does not require that E_h be controlled by a single redox couple; it is also consistent with a multi-reaction mixed potential whose effective

set of contributing reactions and their relative weights remain approximately invariant over the range of oxygen variability. Conversely, a change in slope indicates that the effective reaction set and/or its relative weighting has been reorganized, i.e., oxygen-related electron-transfer pathways have been reweighted relative to other concurrent pathways.

The $\ln[O_2]$–E_h relationship at Site A1 can be translated into mixed-potential terms as follows. A weakened slope suggests a reduced relative weighting of oxygen-coupled interfacial pathways (or an increased contribution of competing pathways), so that changes in oxygen activity produce a smaller shift in the conductance-weighted balance that sets E_{mix}. A systematic positive shift in ΔE_h at a given $\ln[O_2]$ indicates an upward displacement of the mixed-potential baseline, consistent with a reweighting and/or replacement of the effective reaction set toward higher equilibrium-potential contributions under otherwise comparable oxygen levels. The lagged peak in ΔE_h after the EC anomaly relaxed implies that this reorganization persisted beyond the transient ionic-strength/turbidity perturbation, pointing to a slowly evolving internal state that continued to modulate the reaction weights. The partial recovery observed in February 2025 is consistent with gradual re-establishment of the pre-disturbance effective reaction set and its relative weights.

Within Eq. (5), such slow evolution can act through gradual changes in partial polarization conductances and thus in reaction weights, for example via sediment-associated redox buffering, evolving availability of redox-active solutes, and progressive re-establishment of pre-disturbance reaction pathways (Herbel et al., 2007). In the next section, we examine this possibility using a minimal model that isolates the role of slowly varying reaction weights.

We note that electrode-related effects cannot be fully excluded because routine external calibration was not performed. However, the shift showed coherent timing with the documented disturbance, a spatial structure (A1 > A0), and partial recovery in the follow-up profile survey. These features are difficult to reconcile with a simple monotonic sensor-drift scenario and instead support our interpretation that the observed changes primarily reflect system-level reorganization of the interfacial redox processes supplying electrons to the electrode.

4.2 A minimal timescale-separation model for delayed slope changes

Building on the mixed-potential interpretation above, we introduce a minimal timescale-separation model to illustrate how a change in the apparent $\ln[O_2]$–E_h slope can emerge with a delay relative to a fast physical disturbance signature. The model reduces Eq. (4) to two effective branches: an oxygen-sensitive branch and an oxygen-insensitive high-potential branch, whose relative weight varies slowly in time. This toy model is intended to demonstrate mechanistic plausibility (timescale-separated re-weighting under mixed-potential control), rather than to simulate the observed patterns.

We decompose the dynamics into (i) fast oxygen forcing, representing seasonal and short-period fluctuations in O_2 (Fig. 5(a)), and (ii) a slow internal state variable, $s(t)$, representing a pulse-like disturbance and its lingering effect that controls how strongly oxygen-dependent reactions contribute to the mixed potential (Fig. 5(b)). Here, s denotes a latent (unobserved) state variable representing slow changes in the near-electrode redox environment that modulate the relative contributions of interfacial reactions (i.e., G_k), rather than a directly measured chemical species.

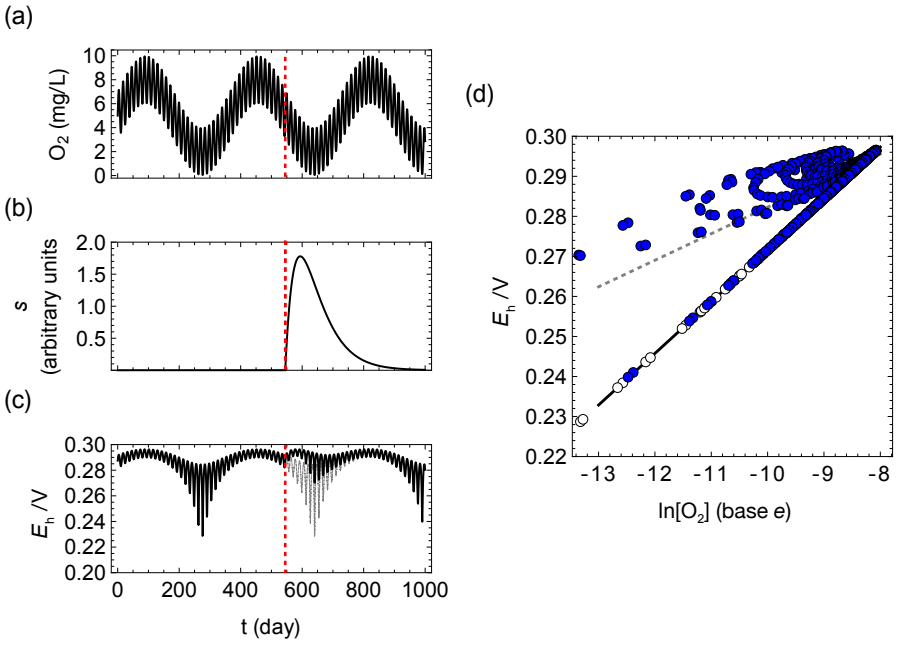

Figure 5. Conceptual two-branch mixed-potential simulation illustrating delayed changes in the apparent $\partial E_h/\partial \ln[\mathrm{O_2}]$ following a pulse-like disturbance. (a) Prescribed $\mathrm{O_2}(t)$ forcing composed of seasonal and short-period fluctuations. (b) A slow latent internal state $s(t)$ (proxy for gradual reconfiguration of the near-electrode redox environment) responding to a pulse forcing applied at $t = t_p$ (red dashed line) and relaxing with timescale τ. (c) Simulated $E_h(t)$ under mixed-potential control. Black: with disturbance-driven evolution of $s(t)$; gray: counterfactual trajectory without disturbance ($u(t) \equiv 0$). (d) Phase plot of E_h versus $\ln[\mathrm{O_2}]$. Open circles indicate the pre-disturbance period ($t < t_p$) and filled circles indicate the post-disturbance period ($t \geq t_p$). Solid and dotted lines show separate linear regressions for the pre- and post-disturbance periods, respectively.

The E_h dynamics are represented as follows:

$$E_h(t) = \big(1 - w(s)\big)\, E_{\mathrm{O_2}}(t) + w(s)\, E_\mathrm{H}, \qquad w(s) = \frac{G_\mathrm{H}(s)}{G_{\mathrm{O_2}} + G_\mathrm{H}(s)}, \tag{7}$$

where $E_{\mathrm{O_2}}(t)$ follows a Nernstian dependence,

$$E_{\mathrm{O_2}}(t) = E^0_{\mathrm{O_2}} + \gamma \ln[\mathrm{O_2}(t)], \tag{8}$$

whereas E_H is assumed insensitive to oxygen on the timescale of interest. The weight factor $w(s)$ increases with a slow latent state $s(t)$ (e.g., through a logistic dependence of G_H on s), so that larger s increases the contribution of the high-potential branch (the specific functional form and parameters are given in the Appendix B).

The slow variable evolves as

$$\frac{ds}{dt} = -\frac{s - s_0}{\tau} + u(t), \tag{9}$$

where $u(t)$ represents a pulse-like disturbance forcing and τ is a relaxation timescale that is long relative to oxygen fluctuations.

This minimal structure yields two key behaviors that mirror our field patterns (Fig. 5(c,d)). First, the instantaneous slope with respect to oxygen is

$$\frac{\partial E_h}{\partial \ln[\mathrm{O_2}]} = \gamma\big(1 - w(s)\big), \tag{10}$$

so that an increase in $w(s)$ produces a reduced apparent $\partial E_h / \partial \ln[\mathrm{O_2}]$ slope (Fig. 5(d)). Second, when $w(s)$ becomes large, E_h can remain high even when $\mathrm{O_2}$ is low (Fig. 5(b,c)), because the high-potential branch dominates the mixed potential. Because s evolves slowly, both the slope reduction and the elevated-E_h residuals can persist and peak after fast disturbance indicators (such as EC) have subsided. Thus, the delayed emergence of the A1 residual shift is consistent with a gradual reconfiguration of the effective redox reaction network.

4.3 Practical implications for monitoring shallow-water redox dynamics

DO is a common target of routine monitoring in aquatic systems, partly because it is directly linked to key ecological processes such as organic-matter degradation and community structure (Bastviken et al., 2004; Connolly et al., 2004; Wang et al., 2008; Franklin, 2014). In contrast, E_h has been used far more selectively, despite the growing availability of robust, field-deployable electrodes suitable for long-term deployment (Vorenhout et al., 2004; Wang et al., 2022). Our results show that neither DO nor E_h alone provides an indicator of system-level redox-network stability, whereas their joint behavior can provide a compact diagnostic of redox-structural change.

Two complementary metrics emerge from co-located, long-term measurements. First, the stability (or breakdown) of the $\ln[\mathrm{O_2}]$–E_h slope serves as an indicator of whether the effective reaction set contributing to the mixed potential remains structurally invariant. Second, baseline-referenced residuals (here, $\Delta E_h = E_h^{\mathrm{obs}} - E_h^{\mathrm{pred}}$, with E_h^{pred} computed from the pooled pre-disturbance regression; Fig. 4b) provide a practical measure of departures from the system-level relationship. Together, these metrics enable detection of disturbance-induced redox-network reconfiguration and subsequent recovery using instrumentation that is already routinely deployed.

At the same time, the mixed-potential nature of E_h imposes clear limits on interpretation. Because multiple combinations of interfacial pathways can yield the same electrode potential, co-monitoring DO and E_h cannot identify the dominant redox couple(s), resolve aqueous speciation, or quantify individual reaction fluxes without complementary measurements of redox-active species. DO–E_h co-monitoring is therefore best viewed not as a substitute for comprehensive geochemical characterization, but as a low-cost tool for qualitative redox-structural shifts in shallow aquatic systems.

5 Conclusions

We revisited field-measured E_h as a mixed potential and asked what mechanistic insight can be extracted from its relationship with a single species, here dissolved oxygen. In a linearized mixed-potential framework, an approximately constant log-linear E_h sensitivity to $\ln[\mathrm{O_2}]$ can arise when the effective set of interfacial reactions contributing to E_h and their relative polarization

conductances remain approximately invariant; such behavior therefore does not require dominance by a single redox couple. Applying this interpretation to a 21-month multi-site time series (July 2022 to March 2024) from a constructed pond, we found that the pre-disturbance $\ln[O_2]$–E_h slope was relatively stable across sites, whereas the site most affected by sediment mobilization (A1) showed a marked weakening and reorganization of the relationship after disturbance. Residuals relative to the pooled pre-disturbance baseline exhibited a pronounced positive shift at A1, peaking after the EC anomaly had largely relaxed, and follow-up vertical profiles in February 2025 indicated partial recovery of the pre-disturbance relationship. Together, these results support the use of the $\ln[O_2]$–E_h slope and baseline residuals as practical, system-level indicators of disturbance-driven redox-network reconfiguration and recovery from co-located sensor measurements, while recognizing that identifying the dominant redox couple still requires concurrent measurements of other redox-active species.

Code and data availability. All raw data (weekly water-quality measurements and vertical profiles) and all analysis scripts written in Wolfram Language (Mathematica 12) will be deposited in a public FAIR repository (e.g., Zenodo or Dryad) upon acceptance. The corresponding DOI will be provided in the final published version. Analyses and simulations were performed in Wolfram Mathematica 12.0 (Wolfram Language). Generative AI tools were used to assist with code editing. All analyses were executed and validated by the authors, who take full responsibility for the results and the final manuscript.

Appendix A: Linearization-based derivation of the mixed potential

For each reaction k, we define the potential E_k at which the partial current vanishes by $i_k(E_k) = 0$. The quantity E_k represents the potential at which electrochemical equilibrium is established between the redox couple involved in reaction k and the electron bath of the electrode. Assuming that the mixed potential lies in the vicinity of each E_k, the partial current $i_k(E)$ can be expanded in a Taylor series around E_k:

$$i_k(E) = i_k(E_k) + \left.\frac{di_k}{dE}\right|_{E=E_k} (E - E_k) + \mathcal{O}((E - E_k)^2). \tag{A1}$$

Since $i_k(E_k) = 0$ by definition, retaining only the linear term yields

$$i_k(E) \simeq G_k(E - E_k) \tag{A2}$$

where

$$G_k \equiv \left.\frac{di_k}{dE}\right|_{E=E_k} \tag{A3}$$

is the partial polarization conductance associated with reaction k, representing the slope of the current-potential response near the equilibrium point. Substituting Eq. (A2) into Eq. (1) gives

$$\sum_k i_k(E) \simeq \sum_k G_k(E - E_k). \tag{A4}$$

On electrodes such as Pt, which possess high catalytic activity and large exchange current densities for many redox reactions, the partial reactions that form the mixed potential are often maintained close to equilibrium (i.e., with small overpotentials $E_{\mathrm{mix}} - E_k$). It is therefore reasonable to assume that E_{mix} lies near each E_k and that Eq. (A4) holds self-consistently at E_{mix}. Hence,

$$\sum_k G_k (E_{\mathrm{mix}} - E_k) = 0. \tag{A5}$$

Rearranging this expression yields

$$E_{\mathrm{mix}} = \frac{\sum_k G_k E_k}{\sum_k G_k} \tag{A6}$$

showing that, in the small-overpotential limit, the mixed potential is given by a conductance-weighted average of the equilibrium potentials E_k of the individual reactions.

Appendix B: Minimal timescale-separation model

B1 Model definition

We constructed a two-branch mixed-potential toy model to demonstrate how an apparent change in the $\ln[\mathrm{O_2}]$–E_h slope can be delayed relative to a fast disturbance signature. The model is intended to show mechanistic plausibility (timescale-separated re-weighting under mixed-potential control), rather than to reproduce the observed magnitudes.

B1.1 Oxygen forcing.

We prescribed an oxygen-activity proxy $a_{\mathrm{O_2}}(t)$ as the sum of seasonal (period P_{season}) and short-period (period P_{fast}) components. The forcing was constructed in concentration units by converting an equivalent DO signal (mg L^{-1}) to mol L^{-1} using the molar mass of $\mathrm{O_2}$ ($M_{\mathrm{O_2}}$):

$$a_{\mathrm{O_2}}(t) = \max\{\epsilon, a_{\mathrm{season}}(t) + a_{\mathrm{fast}}(t)\}, \tag{B1}$$

where

$$a_{\mathrm{season}}(t) = 10^{-3}\,\frac{DO_0 + A_{\mathrm{season}}\sin(2\pi t/P_{\mathrm{season}})}{M_{\mathrm{O_2}}}, \qquad a_{\mathrm{fast}}(t) = 10^{-3}\,\frac{A_{\mathrm{fast}}\sin(2\pi t/P_{\mathrm{fast}})}{M_{\mathrm{O_2}}}. \tag{B2}$$

We imposed a lower bound ϵ to avoid undefined values in $\ln a_{\mathrm{O_2}}$.

B1.2 Slow latent state with pulse-like forcing.

A slow latent state $s(t)$ evolves as

$$\frac{ds}{dt} = -\frac{s - s_0}{\tau} + u(t), \qquad s(0) = s_0, \tag{B3}$$

where the disturbance forcing is

$$u(t) = U_0 \exp\left(-\frac{t - t_p}{\tau_u}\right) H(t - t_p), \tag{B4}$$

and $H(\cdot)$ denotes the Heaviside step function.

B1.3 Reaction weight and two-branch mixed potential.

We mapped $s(t)$ to the effective reaction weight using a logistic function,

$$w(s) = \frac{1}{1 + \exp\{-k(s - s_c)\}}. \tag{B5}$$

The modeled redox potential is a weighted mixture of an oxygen-sensitive branch and an oxygen-insensitive high-potential branch:

$$E_h(t) = \big(1 - w(s(t))\big)\, E_{\mathrm{O_2}}(t) + w(s(t))\, E^0_{\mathrm{H}}. \tag{B6}$$

The oxygen-sensitive branch follows a Nernst-type dependence,

$$E_{\mathrm{O_2}}(t) = E^0_{\mathrm{O_2}} + \gamma \ln a_{\mathrm{O_2}}(t), \tag{B7}$$

where γ is treated as a slope-scale parameter (set to RT/F in our demonstration run; Table A3). A no-perturbation reference trajectory was obtained by fixing the weight at $w(s_0)$:

$$E_h^{\mathrm{wop}}(t) = \big(1 - w(s_0)\big)\, E_{\mathrm{O_2}}(t) + w(s_0)\, E^0_{\mathrm{H}}. \tag{B8}$$

B1.4 Instantaneous slope.

Because E_h is affine in $\ln a_{\mathrm{O_2}}$ for fixed w, the instantaneous slope is

$$\frac{\partial E_h}{\partial \ln a_{\mathrm{O_2}}} = \gamma\big(1 - w(s(t))\big), \tag{B9}$$

so that an increase in w yields an apparent weakening of the $\ln[\mathrm{O_2}]$–E_h sensitivity.

B2 Numerics and parameters

We solved the ODE for $s(t)$ using NDSolve over $t \in [0, t_{\max}]$ and computed $E_h(t)$ from the closed-form expressions above. The logistic weight $w(s)$ was evaluated along the numerical trajectory $s(t)$. All parameter values used for the demonstration run are listed in Table A3.

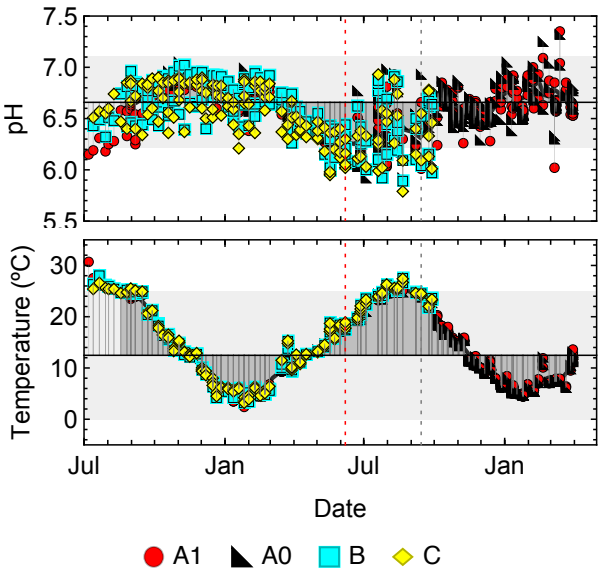

Figure A1. Time series of (a) pH and (b) water temperature measured in situ at the four monitoring sites (A1, A0, B, and C) from July 2022 to March 2024. Symbols show weekly measurements at different depths at each site. Vertical dashed lines mark the operational change points adopted in the main text (red: disturbance onset associated with channel excavation; gray: transition from the EC amplification phase to the relaxation phase). Solid lines and shaded bands indicate the mean and mean ± 1.96 SD range during pre-disturbance regime calculated from all sites.

Table A1. Specifications of instruments and sensors used for in situ monitoring.

Parameter	Instrument / model	Range	Resolution	Stated accuracy / notes
Dissolved oxygen (mg L^{-1}; %)	LAQUA-WQ310 + optode 300-D-2	0.00–20.00 mg L^{-1} 0–200.0 %	0.01 mg L^{-1} 0.1 %	$\pm$0.2 mg L^{-1}; $\pm$2 % (DO%)
ORP	LAQUA-WQ310 + 9300-10D (Pt/Ag–AgCl)	-2000 to $+2000$ mV	0.1 mV (|ORP| $\leq$ 999.9) 1 mV (otherwise)	repeatability: $\pm$0.1 mV (\|ORP\|$\leq$999.9); $\pm$1 mV (otherwise)
Electrical conductivity	LAQUA-WQ310 + 300-C-2 (300-4C-C)	auto-range (0.000–2000 mS cm^{-1})	4 significant digits	repeatability: $\pm$0.5 % FS; $\pm$1.5 % FS (high range)
pH	PRN-41	0.00–14.00	0.01	(specification not stated in accessible manual excerpt)
Water temperature	built-in (probe)	-30.0 to $+130.0$ °C	0.1 °C	repeatability: $\pm$0.5 °C

Table A2. Linear regression summaries for the relationship between E_h (V vs. SHE) and $\ln[O_2]$ (natural logarithm, base e). We approximated the activity of O_2 by its molar concentration; therefore, data with DO $= 0$ were excluded from regression because $\ln[O_2]$ is undefined. All sites indicates pooled data across sites. The pre-disturbance regime was defined based on the EC change-point analysis (see main text).

Dataset	Intercept (V)	SE	Slope (V)	SE	Adjusted R^2	n
(a) Full observation period						
All sites	1.195	0.0345	0.0820	0.00304	0.401	1086
A1	1.284	0.0597	0.0834	0.00525	0.372	425
A0	1.166	0.0408	0.0796	0.00363	0.572	359
B	1.139	0.0678	0.0844	0.00597	0.547	166
C	0.991	0.0763	0.0747	0.00666	0.481	136
(b) Pre-perturbation regime						
All sites	1.181	0.0438	0.0859	0.00389	0.448	599
A1	1.433	0.0783	0.1045	0.00688	0.523	210
A0	1.037	0.0685	0.0723	0.00603	0.476	158
B	1.108	0.0840	0.0813	0.00761	0.473	127
C	1.118	0.0997	0.0862	0.00898	0.469	104

Table A3. Parameter values used in the minimal timescale-separation simulation (Fig. 5).

Symbol	Meaning	Value	Unit
$t_{\max}$	simulation length	1000	d
DO_0	baseline DO level (seasonal component)	5	mg L^{-1}
A_{season}	seasonal amplitude	3	mg L^{-1}
A_{fast}	short-period amplitude	2	mg L^{-1}
P_{season}	seasonal period	365	d
P_{fast}	short period	14	d
M_{O_2}	molar mass of oxygen	31.998	g mol^{-1}
ϵ	lower bound for a_{O_2}	10^{-12}	mol L^{-1}
t_p	disturbance onset time	$365 + 180$	d
U_0	pulse forcing magnitude	10^{-4}	(unit of s) d^{-1}
τ_u	pulse decay timescale	40	d
τ	relaxation timescale of s	60	d
s_0	baseline latent state	10^{-6}	(unit of s)
k	logistic steepness	10^3	(unit of s)$^{-1}$
s_c	logistic threshold	10^{-5}	(unit of s)
$E^0_{O_2}$	baseline of O_2 branch	0.5	V
E^0_H	high-potential branch level	0.3	V
γ	slope scale in E_{O_2}	RT/F	V
R	gas constant	8.31	J mol^{-1} K^{-1}
T	temperature	298	K
F	Faraday constant	96485	C mol^{-1}

Author contributions. M.S. conceived the theoretical framework and designed the study. M.I. and K.I. designed the experimental setup and installed the logging devices. K.M. conducted the monitoring, curated the datasets, and performed the initial formal analyses. M.S. led the analysis design, interpreted the results, and wrote the manuscript with input from all authors.

Competing interests. The authors declare that they have no conflict of interest.

Acknowledgements. This study was supported by JSPS KAKENHI Grant Numbers 24K01844 (MS, MI, and KI) and 24H01514 (MS), and by the Iwatani Naoji Foundation (MS). The authors are grateful for comments from Ryuhei Nakamura, Hideshi Ooka, and Hiroyuki Kashima. AI-assisted language tools were used to improve grammar and readability. All analyses were performed and validated by the authors, who take full responsibility for the results and interpretations.

References

Aladejana, J. A., Kalin, R. M., Sentenac, P., and Hassan, I.: Assessing the Impact of Climate Change on Groundwater Quality of the Shallow Coastal Aquifer of Eastern Dahomey Basin, Southwestern Nigeria, Water, 12, 224, https://doi.org/10.3390/w12010224, 2020.

Auqué, L., Gimeno, M., Gómez, J., and Nilsson, A.-C.: Potentiometrically Measured Eh in Groundwaters from the Scandinavian Shield, Applied Geochemistry, 23, 1820–1833, https://doi.org/10.1016/j.apgeochem.2008.02.016, 2008.

Bastviken, D., Persson, L., Odham, G., and Tranvik, L.: Degradation of Dissolved Organic Matter in Oxic and Anoxic Lake Water, Limnology and Oceanography, 49, 109–116, https://doi.org/10.4319/lo.2004.49.1.0109, 2004.

Borch, T., Kretzschmar, R., Kappler, A., Cappellen, P. V., Ginder-Vogel, M., Voegelin, A., and Campbell, K.: Biogeochemical Redox Processes and Their Impact on Contaminant Dynamics, Environmental Science & Technology, 44, 15–23, https://doi.org/10.1021/es9026248, 2010.

Bowman, G., Harris, G., Kirk, M., and Jin, Q.: A Data-Driven Simplified Nernst Equation for Estimating Reduction Potentials in Groundwater from pH and Temperature, Groundwater, 63, 725–735, https://doi.org/10.1111/gwat.70010, 2025.

Connolly, N. M., Crossland, M. R., and Pearson, R. G.: Effect of Low Dissolved Oxygen on Survival, Emergence, and Drift of Tropical Stream Macroinvertebrates, Journal of the North American Benthological Society, 23, 251–270, https://doi.org/10.1899/0887-3593(2004)023<0251:EOLDOO>2.0.CO;2, 2004.

Cuoco, E., Viaroli, S., Paolucci, V., Mazza, R., and Tedesco, D.: Fe and As Geochemical Self-Removal Dynamics in Mineral Waters: Evidence from the Ferrarelle Groundwater System (Riardo Plain, Southern Italy), Environmental Geochemistry and Health, 44, 2065–2082, https://doi.org/10.1007/s10653-021-00891-5, 2022.

Franklin, P.: Dissolved Oxygen Criteria for Freshwater Fish in New Zealand: A Revised Approach, New Zealand Journal of Marine and Freshwater Research, 48, 112–126, https://doi.org/10.1080/00288330.2013.827123, 2014.

Grenthe, I., Stumm, W., Laaksuharju, M., Nilsson, A., and Wikberg, P.: Redox Potentials and Redox Reactions in Deep Groundwater Systems, Chemical Geology, 98, 131–150, https://doi.org/10.1016/0009-2541(92)90095-M, 1992.

Grundl, T.: A Review of the Current Understanding of Redox Capacity in Natural, Disequilibrium Systems, Chemosphere, 28, 613–626, https://doi.org/10.1016/0045-6535(94)90303-4, 1994.

Hayashi, M.: Temperature-Electrical Conductivity Relation of Water for Environmental Monitoring and Geophysical Data Inversion, Environmental Monitoring and Assessment, 96, 119–128, https://doi.org/10.1023/B:EMAS.0000031719.83065.68, 2004.

Herbel, M. J., Suarez, D. L., Goldberg, S., and Gao, S.: Evaluation of Chemical Amendments for pH and Redox Stabilization in Aqueous Suspensions of Three California Soils, Soil Science Society of America Journal, 71, 927–939, https://doi.org/10.2136/sssaj2006.0209, 2007.

Ioka, S., Sakai, T., Igarashi, T., and Ishijima, Y.: Determination of Redox Potential of Sulfidic Groundwater in Unconsolidated Sediments by Long-Term Continuous in Situ Potentiometric Measurements, Environmental Monitoring and Assessment, 178, 171–178, https://doi.org/10.1007/s10661-010-1680-4, 2011.

Jahangir, M., Johnston, P., Khalil, M., and Richards, K.: Linking Hydrogeochemistry to Nitrate Abundance in Groundwater in Agricultural Settings in Ireland, Journal of Hydrology, 448–449, 212–222, https://doi.org/10.1016/j.jhydrol.2012.04.054, 2012.

Lau, M. P., Niederdorfer, R., Sepulveda-Jauregui, A., and Hupfer, M.: Synthesizing Redox Biogeochemistry at Aquatic Interfaces, Limnologica, 68, 59–70, https://doi.org/10.1016/j.limno.2017.08.001, 2018.

Lindberg, R. D. and Runnells, D. D.: Ground Water Redox Reactions: An Analysis of Equilibrium State Applied to Eh Measurements and Geochemical Modeling, Science, 225, 925–927, https://doi.org/10.1126/science.225.4665.925, 1984.

Linnik, P., Osadchyi, V., Osadcha, N., and Linnik, R.: Redox Potential as an Important Characteristic of the Chemical and Biological State of Surface Waters (Review), Chemistry and Ecology, 39, 640–672, https://doi.org/10.1080/02757540.2023.2225496, 2023.

Luther, G. W.: Inorganic Chemistry for Geochemistry and Environmental Sciences: Fundamentals and Applications, John Wiley & Sons, Ltd, Chichester, UK, ISBN 978-1-118-85143-2 978-1-118-85137-1, https://doi.org/10.1002/9781118851432, 2016.

McAleer, E., Coxon, C., Richards, K., Jahangir, M., Grant, J., and Mellander, Per.E.: Groundwater Nitrate Reduction versus Dissolved Gas Production: A Tale of Two Catchments, Science of The Total Environment, 586, 372–389, https://doi.org/10.1016/j.scitotenv.2016.11.083, 2017.

Ramesh Kumar, A. and Riyazuddin, P.: Seasonal Variation of Redox Species and Redox Potentials in Shallow Groundwater: A Comparison of Measured and Calculated Redox Potentials, Journal of Hydrology, 444–445, 187–198, https://doi.org/10.1016/j.jhydrol.2012.04.018, 2012.

Schlesinger, W. H. and Bernhardt, E. S.: Wetland Ecosystems, in: Biogeochemistry, pp. 233–274, Elsevier, ISBN 978-0-12-385874-0, https://doi.org/10.1016/B978-0-12-385874-0.00007-8, 2013.

Seto, M. and Akagi, T.: Influence of Snow on Iron Release from Soil, GEOCHEMICAL JOURNAL, 39, 173–183, https://doi.org/10.2343/geochemj.39.173, 2005.

Shrestha, R. K. and Lal, R.: Changes in Physical and Chemical Properties of Soil after Surface Mining and Reclamation, Geoderma, 161, 168–176, https://doi.org/10.1016/j.geoderma.2010.12.015, 2011.

Silva, M. M. V. G., Gomes, E. M. C., Isaías, M., Azevedo, J. M. M., and Zeferino, B.: Spatial and Seasonal Variations of Surface and Groundwater Quality in a Fast-Growing City: Lubango, Angola, Environmental Earth Sciences, 76, 790, https://doi.org/10.1007/s12665-017-7149-9, 2017.

Stefánsson, A., Arnórsson, S., and Sveinbjörnsdóttir, Á. E.: Redox Reactions and Potentials in Natural Waters at Disequilibrium, Chemical Geology, 221, 289–311, https://doi.org/10.1016/j.chemgeo.2005.06.003, 2005.

Stumm, W. and Morgan, J. J.: Aquatic Chemistry: Chemical Equilibria and Rates in Natural Waters, Environmental Science and Technology, J. Wiley & sons, New York Chichester Brisbane [etc.], 3rd ed edn., ISBN 978-0-471-51184-7, 1996.

Tandon, P. K. and Singh, S. B.: Redox Processes in Water Remediation, Environmental Chemistry Letters, 14, 15–25, https://doi.org/10.1007/s10311-015-0540-4, 2016.

Teasdale, P. R., Minett, A. I., Dixon, K., Lewis, T. W., and Batley, G. E.: Practical Improvements for Redox Potential (EH) Measurements and the Application of a Multiple-Electrode Redox Probe (MERP) for Characterising Sediment in Situ, Analytica Chimica Acta, 367, 201–213, https://doi.org/10.1016/S0003-2670(98)00171-8, 1998.

Violante, A., Cozzolino, V., Perelomov, L., Caporale, A., and Pigna, M.: Mobility and Bioavailability of Heavy Metals and Metalloids in Soil Environments, Journal of soil science and plant nutrition, 10, https://doi.org/10.4067/S0718-95162010000100005, 2010.

Vorenhout, M., Van Der Geest, H. G., Van Marum, D., Wattel, K., and Eijsackers, H. J. P.: Automated and Continuous Redox Potential Measurements in Soil, Journal of Environmental Quality, 33, 1562–1567, https://doi.org/10.2134/jeq2004.1562, 2004.

Wang, S., Jin, X., Bu, Q., Jiao, L., and Wu, F.: Effects of Dissolved Oxygen Supply Level on Phosphorus Release from Lake Sediments, Colloids and Surfaces A: Physicochemical and Engineering Aspects, 316, 245–252, https://doi.org/10.1016/j.colsurfa.2007.09.007, 2008.

Wang, X., Wu, Y., Chen, N., Piao, H., Sun, D., Ratnaweera, H., Maletskyi, Z., and Bi, X.: Characterization of Oxidation-Reduction Potential Variations in Biological Wastewater Treatment Processes: A Study from Mechanism to Application, Processes, 10, 2607, https://doi.org/10.3390/pr10122607, 2022.

Whitfield, M.: Eh as an Operational, Parameter in Estuarine Studies, Limnology and Oceanography, 14, 547–558, https://doi.org/10.4319/lo.1969.14.4.0547, 1969.

Whitfield, M.: Thermodynamic Limitations on the Use of the Platinum Electrode in *Eh* Measurements, Limnology and Oceanography, 19, 857–865, https://doi.org/10.4319/lo.1974.19.5.0857, 1974.

Winkel, L., Berg, M., Stengel, C., and Rosenberg, T.: Hydrogeological Survey Assessing Arsenic and Other Groundwater Contaminants in the Lowlands of Sumatra, Indonesia, Applied Geochemistry, 23, 3019–3028, https://doi.org/10.1016/j.apgeochem.2008.06.021, 2008.

Włodarczyk, T., Szarlip, P., Brzezińska, M., and Kotowska, U.: Redox Potential, Nitrate Content and pH in Flooded Eutric Cambisol during Nitrate Reduction, Research in Agricultural Engineering, 53, 20–28, https://doi.org/10.17221/2132-RAE, 2007.

Yu, S., Yu, G. B., Liu, Y., Li, G. L., Feng, S., Wu, S. C., and Wong, M. H.: Urbanization Impairs Surface Water Quality: Eutrophication and Metal Stress in the Grand Canal of China, River Research and Applications, 28, 1135–1148, https://doi.org/10.1002/rra.1501, 2012.

Zhai, J., Zou, J., He, Q., Ning, K., and Xiao, H.: Variation of Dissolved Oxygen and Redox Potential and Their Correlation with Microbial Population along a Novel Horizontal Subsurface Flow Wetland, Environmental Technology, 33, 1999–2006, https://doi.org/10.1080/09593330.2012.655320, 2012.